Towards additive manufacturing of dielectric accelerating structures

Journal of Physics: Conference Series **1596** (2020) 012020 doi:10.1088/1742-6596/1596/1/012020

Towards additive manufacturing of dielectric accelerating structures

Max Kellermeier[1,3], Simon Zinsli[2], Ulrich Dorda[1], Rasmus Ischebeck[2], Jonas Lehmann[2], Benedikt Hermann[2], Klaus Flöttmann[1], François Lemery[1], Hannes Dinter[1], Csaba Lombosi[2], Marijo Magjar[2], Lukas Stingelin[2], Wolfgang Hillert[3] and Ralph Aßmann[1]

[1] Deutsches Elektronen-Synchrotron (DESY), Notkestr. 85, D-22607 Hamburg, Germany
[2] Paul Scherrer Institut (PSI), CH-5232 Villigen, Switzerland
[3] University of Hamburg, Mittelweg 177, D-20148 Hamburg, Germany

E-mail: max.kellermeier@desy.de

Abstract. Additive manufacturing techniques such as stereolithography have developed rapidly in the last decade and provide the ability to simplify prototyping and manufacturing of unique, complex structures. For the application to dielectric accelerating structures a precise knowledge of the dielectric permittivity of the material is essential to the design. Here we present the characterization of commercially available polymers used in stereolithographic manufacturing by means of refractive index and absorption in the frequency range from 220 GHz to 330 GHz, and around 60 GHz. Vacuum compatibility has been tested with respect to achievable pressure level and residual gas mass spectra. In the future the polymer properties will be applied to designs of accelerating structures as well as couplers for terahertz-driven dielectric accelerator components.

1. Introduction

Additive manufacturing, often denoted as 3D printing, not only gained a lot of interest in the general public in the last few years but due to technological advances also in the accelerator community. Progress in printable materials paved the road for 3D printed beam position monitors [1], while smaller feature sizes are especially interesting for novel laser-driven accelerators, such as the woodpile structure printed with a Nanoscribe [2]. While these specialized printers at the forefront of 3D printing are complex and expensive, also conventional polymer printers allow for new mechanical designs which may otherwise be impractical, such as tapered dielectric loaded waveguides for low energy electron acceleration [3] or step-wise loaded waveguides for passive longitudinal phase space synthesis [4].

The optical properties of printable polymers for the well-known fused deposition modeling (FDM) have been studied extensively in the past [5] in order to manufacture waveguides and splitters [6], metamaterial lenses, gratings and other optical components for terahertz frequencies [7, 8, 9]. However, these printers are limited in vertical and transverse resolution to about 100 µm, depending on the nozzle size, the print head movement and the layer height. Optical printing technologies such as stereolithography (SLA) and digital light processing (DLP) allow for smaller feature sizes in the order of tens of microns. A limitation of these printers is the material as the monomeric resin has to be mixed with chemical photo initiators and light blockers. Therefore,

the material parameters such as dielectric permittivity and refractive index, respectively, depend on the constituents of the printable resin. Here, we study the material parameters of proprietary SLA-printing resins at 60 GHz and in the range of 220 GHz to 330 GHz, with the aim for applications in dielectric laser accelerators. The refractive index and absorption of FormLabs High Temperature and FormLabs Clear resins is measured by means of refraction on a printed prism. Asiga FusionGRAY is studied in the millimeter wave range with respect to the phase shift caused by the dielectric permittivity.
For applications in accelerator environments vacuum compatibility plays a crucial role. Tests with pretreated samples of FormLabs High Temperature resin are conducted in a Residual Gas Analyzer (RGA).

2. Vacuum compatibility

Particle accelerators need to operate in a vacuum to avoid collisions of the accelerated particles with gas molecules. Here, we study the applicability of polymers for use in an external vacuum chamber with respect to outgassing of small molecules which may degrade the vacuum. To lower the outgassing rate from the polymer surface, samples with different temperature treatments have been prepared prior to the RGA test, see table 1. All parts were printed under same conditions and have a shape with 6.6 cm^2 total surface area. An aluminum part of the same shape is used as a reference.
Each sample is pumped in the RGA up to 100 h. Figure 1(a) shows the leak rate during the pumping process. While the samples baked in ambient and nitrogen environment performed very similar or only slightly better than the non-baked sample, the temperature treatment in rough vacuum is promising. Still, the polymer cannot reach the same performance as aluminum. In all five cases the mass spectrum of the baked samples showed a lower ion current compared to the untreated one. Here, again, the heat treatment in the rough vacuum environment is the most promising one. Figure 1(b) shows a comparison of the mass spectrum between the resin and aluminum. As the peaks occur at the same mass units they indicate a not very clean vacuum chamber in case of the second measurement.
Although the hydrocarbon constituents are not negligible in the mass spectrum the out-gassing rate is sufficiently low to apply the material in the ultra-high vacuum environment of an accelerator. Currently, a lens made of FormLabs High Temperature resin is used in a vacuum chamber of SwissFEL at the Paul Scherrer Institut.

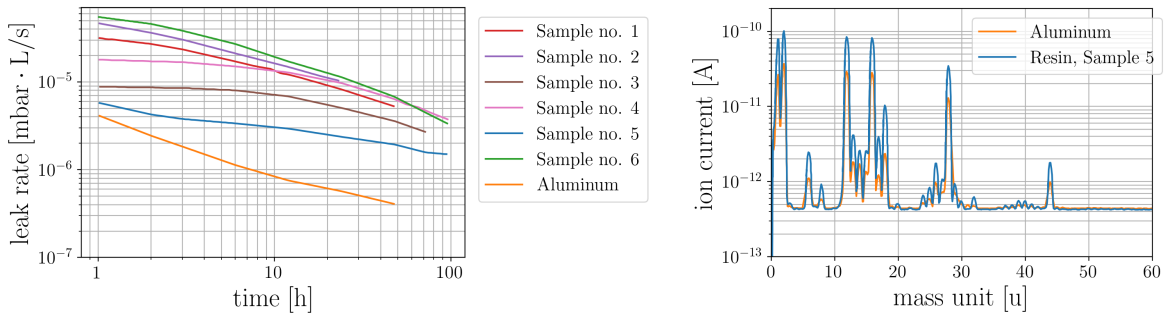

(a) (b)

Figure 1: (a) Leak rate during the pumping of different samples in the RGA. (b) Mass spectrum of sample with the most promising baking treatment together with the spectrum of the aluminum sample.

Table 1: Temperature treatment of the six printed samples before vacuum test. The first sample was not baked while the next three samples were heated to the same temperature but baked for different times. During the treatment of sample no. 5 the oven was roughly pumped, while in case of the last sample it was flooded with nitrogen.
The pressure reached after 48 h is only a relative measure as it depends on the RGA and the pump rate. An aluminum sample pumped under the same conditions is used as a reference.

Sample	Temp. [°C]	Baking time [min]	Environment	Pressure after 48 h [mbar]
1	0	0	ambient	5×10^{-8}
2	235	90	ambient	1×10^{-7} after 24 h
3	235	180	ambient	4×10^{-8}
4	235	360	ambient	6×10^{-8}
5	175	297	rough vacuum	2×10^{-8}
6	175	297	purged nitrogen	6×10^{-8}
Al	–	–	–	5×10^{-9}

3. 60 GHz fixed angle method for prism-shaped specimen

3.1. Setup and Method

An Acconeer 111 pulsed transceiver operating at 60 GHz radiofrequency (RF) is used as a signal generator and detector. Due to the low directivity the transceiver's antenna is extended by a 3D-printed parabolic horn made of copper containing PLA. The horn was sandblasted in order to improve its surface conductivity. A printed prismatic sample is placed on a rotational stage right in front of the antenna, as shown in figure 2(a). In a fixed distance a retroreflector is mounted on a movable arm. For one angular position of the prism, the retroreflector angle is scanned while recording the reflected intensity on the transceiver. The angular position of maximal signal is extracted for the analysis. The inset in figure 2(a) shows such an intensity profile measured from 10° to 70° in steps of 0.5°, resulting in a measured deflection angle $\delta \approx 50°$.
The refractive index is determined via the fixed angle of incidence method [10], based on ray optics. In the geometrical sketch in figure 2(a) the angles γ of the printed equilateral prism, and rotational position ε are known, while the deflection δ is measured with the scan. Snell's law and trigonometry provide a system of equations which can be solved for the unknown refractive index n.
The same setup has been used for absorption measurements with three slabs of 1 cm thickness,

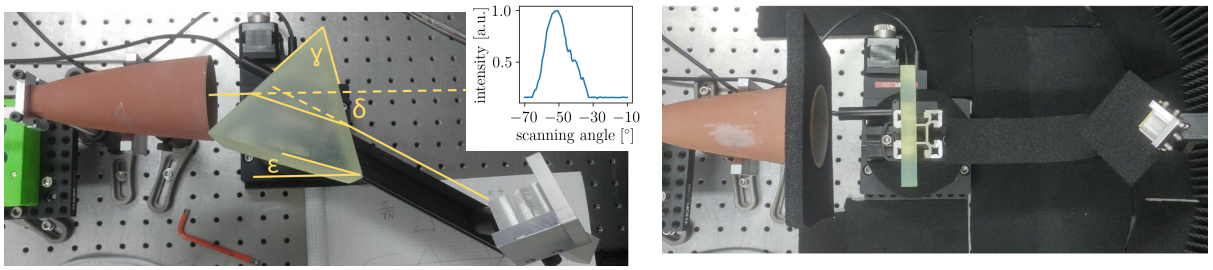

(a) (b)

Figure 2: (a) Setup of the prism-based fixed angle measurement. Inset: Measured intensity profile over a range of 60° with a Formlabs High Temperature resin printed prism of $\gamma = 60°$. (b) The same setup is used to measure absorption through slabs.

figure 2(b). From the attenuation of the reflected intensity the absorption α is computed based on Beer-Lambert's law. By stacking the slabs, measurements with different wall thicknesses are carried out.

3.2. Results

In case of FormLabs Clear resin and FormLabs High Temperature resin, prisms with two prismatic angles, $\gamma = 60°$ and $\gamma = 30°$, are studied. To determine the statistical uncertainty 40 scans are carried out. For Asiga FusionGRAY, 16 scans are conducted with a printed 30° prism. Table 2 lists the results for the refractive indices, including the statistical uncertainty for the FormLabs resins as well as the measured absorption.
Both resins show a refractive index similar to other polymers [5]. The value for the High Temperature resin is slightly larger by about 2.5 % which is very close to the uncertainty of 2.1 %.
The absorption is low in comparison to other polymers [11]. It was not possible to measure below the given estimate in table 2 due to the limitation of the setup.

Table 2: Refractive index and absorption at 60 GHz of the two FormLabs resins, and Asiga FusionGRAY. Absorption of Asiga FusionGRAY is not tested.

Resin	Refractive Index n	Absorption α [dB/cm]
FormLabs Clear	1.609 ± 0.024	≈ 0.04
FormLabs High Temp.	1.648 ± 0.036	≈ 0.04
Asiga FusionGRAY	1.670 ± 0.015	-

4. Free space S-parameter measurement at millimeter waves

4.1. Quasi Gaussian optics setup

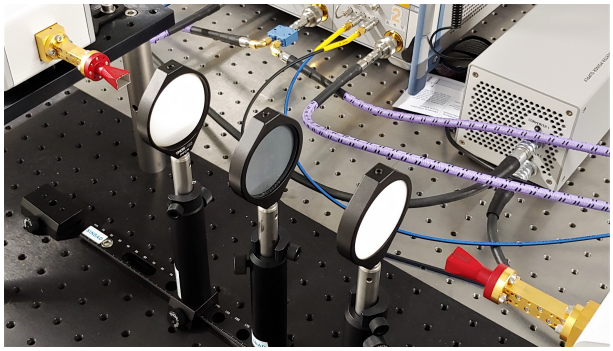

Figure 3: Vector Network Analyzer (VNA)-based quasi-optical Gaussian setup for S-parameter measurement.

A Rohde & Schwarz ZVA67 VNA is used for measuring the scattering parameters. The frequency range is extended to 220 GHz to 330 GHz using two ZC330 frequency converters. A standard gain horn antenna is attached to the waveguide port of each converter and they are placed opposite to each other in a distance of $L_{\text{tot}} = 30\,\text{cm}$ along an optical rail, shown in figure 3. Two identical PTFE lenses with $f = 75\,\text{mm}$ focal length provide a symmetrical quasi Gaussian setup. The first lens is placed in distance of the focal length from the first antenna

in order to collimate the diverging beam. The second lens is placed in distance of f from the second antenna in order to focus the collimated beam from the first antenna into the second one. The total length of 30 cm corresponds to four times the focal length and the material sample will be placed in the symmetry plane. The initial $1/e^2$ half beam width at center frequency is read off from the radiation pattern at $-8.7\,\mathrm{dB}$ as $\theta = 12°$ and results in an beam radius of 16 mm incident on the sample. Due to the lack of rotational symmetry of the antenna's aperture the divergence differs between the E-plane and H-plane, but for modeling the beam propagation the differences are negligible.
In order to extract the material parameters from S-parameter measurements the incident radiation on the sample has to have plane wave characteristic. This is satisfied in the far field, which requires (i) $L_{\mathrm{tot}}/2 > \lambda$ (ii) $L_{\mathrm{tot}}/2 > D$ (iii) $L_{\mathrm{tot}}/2 > (2D^2)/\lambda$. Here $\lambda \approx 1\,\mathrm{mm}$ is the center wavelength and $D = 11\,\mathrm{mm}$ is the largest side of the antenna's aperture. In the current setup the last condition is not sufficiently satisfied. The consequences will be discussed later.
A gold mirror is used to align the lenses with respect to the common focal plane. The time domain transform implemented on the VNA allows for proper positioning of the mirror. When the responses of both surfaces in $S_{11}(t)$ and $S_{22}(t)$ overlap the mirror is centered between the horns. By moving it by half of its thickness the mirror's surface is centered instead of the bulk. The first lens is placed between the antenna and the mirror, and the position is adjusted until the reflected signal $S_{11}(f)$ is maximal. In this case the mirror is in focus of the collimated beam. The same procedure is repeated for the second lens. Finally, the sample is aligned along the optical axis in the same way as the gold mirror.

4.2. Free space calibration techniques
The goal of the calibration is, on the one hand, to eliminate systematic errors within the cables, the VNA and the frequency extenders. On the other hand, the calibration defines the reference plane for the S-parameters. However, no calibration standards exist for free space measurements so the free space calibration has to be performed offline. Figure 4 shows the erroneous network modeling the free space measurements. When calibrated up to the waveguide ports the measured S-parameters include contributions from the antennas, the quasi-Gaussian optics, the support structures and the surrounding environment.
A common method for microwave measurements is the Thru-Reflect-Line (TRL) calibration [12, 13, 14, 15]. The reflect standard is realized as a metallic mirror placed in the common focal plane. The thru and the line standards both correspond to a sample-free measurement, but with different electrical lengths. The line standard has to be about a quarter wavelength longer than the thru standard. This requires the precise displacement of one of the antennas by about

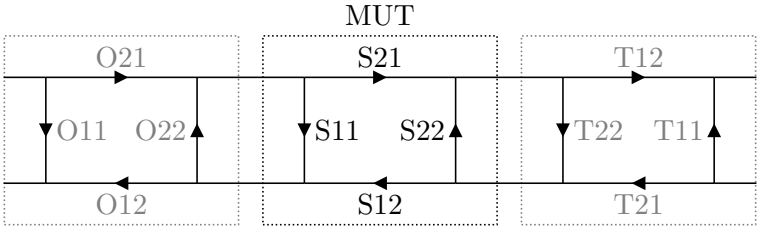

Figure 4: Signal flow graph of the 8-term error model. Here, S denotes the desired S-parameters of the Material Under Test (MUT) while O and T denote the error networks from the wave guide ports to the slab surfaces, including the antenna flange and aperture, the lenses, the mounting structures and air, as well as alignment errors.

250 µm which in turn affects the beam propagation [16]. As this might be critical it is more advantageous to calibrate without a mechanical change of the setup.
One alternative is the so-called Gated-Reflect-Line (GRL) method [17, 18] which uses a two-step approach. First, a Thru-Open-Short-Match (TOSM) calibration is applied to the waveguide ports. Second, measurements of the reflect and the line standard in free space are combined with time domain gates around the antenna responses in order to move the calibration plane to the sample surface. The gating is used to correct for systematic errors coming from the antennas. This can only be done in a lens-free setup as the lens surface introduces strong reflections. The GRL method cannot be used to fully determine the system imperfections.
Nevertheless a simplified method using the same calibration standards is applicable. Instead of determining the parameters of the full error networks O and T, the measured S-parameters are normalized separately afterwards [19, 20]. The reflection parameter $S_{11}^{(m)}$ of the material measurement is normalized by $S_{11}^{(r)}$ from the reflect standard measurement, while the transmission parameter is normalized by the thru standard measurement $S_{21}^{(t)}$. Gating of the sample response is required afterwards since multiple reflections in the setup are not properly normalized due to the introduced delay.
The Line-Network-Network (LNN) self-calibration [16] does not require any calibration measurement. The sample is measured at three different positions of a fixed distance l_{lnn} along the optical axis. Matrix formalism and properties of similarity transforms are applied to eliminate the error contributions from the measurements. The distance between the sample positions has to be much smaller than the Rayleigh range of the beam, $l_{lnn} \ll z_r$, in order to satisfy the assumption of a constant phase front on the sample. In the current setup, the incident beam has a Rayleigh length of $z_r = 600\,\mathrm{mm}$.
For the measurements the simplified thru-reflect method and the LNN self-calibration were applied.

4.3. Material parameter extraction
The most general method to extract the permittivity ε_r and the permeability μ_r from the S-parameters is the well-known Nicolson-Ross-Weir (NRW) method [21, 22]. It aims for inverting the analytical relations

$$S_{11}(\varepsilon_r, \mu_r) = \frac{(1-T^2)\Gamma}{1-\Gamma^2 T^2}, \quad S_{21}(\varepsilon_r, \mu_r) = \frac{(1-\Gamma^2)T}{1-\Gamma^2 T^2}, \tag{1}$$

with

$$\Gamma = \frac{Z - Z_0}{Z + Z_0}, \quad T = e^{ik_s d}, \quad Z = \sqrt{\frac{\mu_0 \mu_r}{\epsilon_0 \epsilon_r}}, \quad k_s = \omega\sqrt{\epsilon_0 \mu_0 \epsilon_r \mu_r}, \tag{2}$$

where Γ and T are the reflection and the transmission coefficient of a half-space, Z and Z_0 are the material and the free space impedance, and k_s is the wave vector in the material slab of thickness d. $\epsilon_r = \Re\epsilon_r + i\Im\epsilon_r$ and μ_r are the complex relative permittivity and permeability, respectively. However, the analytic expression is very sensitive to uncertainties in the measured phase, diverges in multiple integers of half wavelength in the sample and becomes algebraic unstable [19]. In addition the wave vector k_s is not unique due to the branch ambiguity of the complex logarithm [23].
Numerical methods are often more stable. The relation between S-parameters and the material parameters are re-expressed as a root-finding problem of an error function $F(\varepsilon_r; S_{11}, S_{21})$ which is numerically solved by the Newton-Raphson algorithm [14, 19]. A disadvantage is the limitation to one material parameter, ε_r, assuming a non-magnetic sample, $\mu_r = 1$. In case of polymers

this is a valid assumption.
Here the transmission-only method is applied which solves the equation

$$F_{TO} \equiv S_{21}\left(\varepsilon_r \cos(\nu) + i\sqrt{\frac{\varepsilon_r}{4}}(1+\varepsilon_r)\sin(\nu)\right) - \varepsilon_r \stackrel{!}{=} 0 \tag{3}$$

for ε_r, where $\nu = d(\omega/c)\sqrt{\varepsilon_r}$. Due to the branch ambiguity a good guess for the start value of the iterative method has to be applied. Alternatively, measurements of different sample thicknesses allow for solving the ambiguity.

4.4. Results

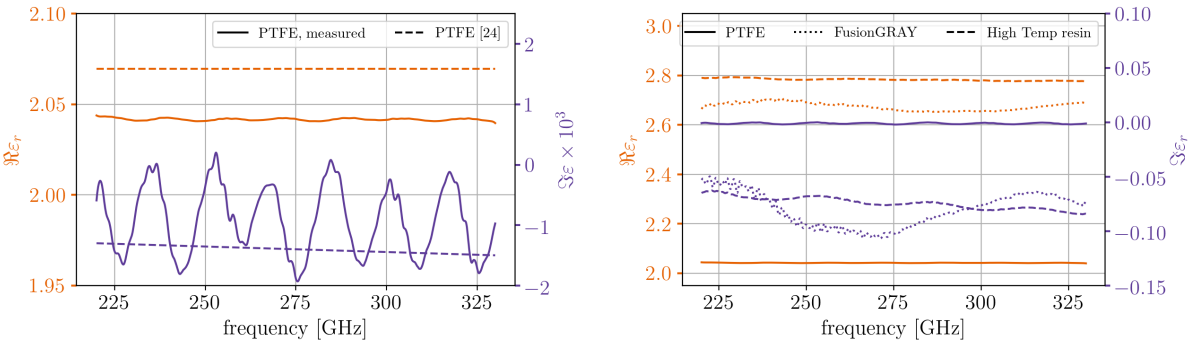

(a) (b)

Figure 5: Real and imaginary part of the relative complex permittivity of (a) polytetrafluoroethylene (PTFE), including the expected permittivity according to [24], and (b) different printed materials, determined with S-parameter measurements. In both cases oscillations across the frequency range are observed. These are not physical and attributed to systematic errors.

Due to its wide use in terahertz applications the dielectric permittivity of PTFE is measured as a reference. After the calibration measurements, one with an empty sample holder and one with the mirror, a slab of (6.38 ± 0.01) mm thickness is mounted in the focal plane. The S-parameters are measured at 10 000 linearly spaced frequency points between 220 GHz and 330 GHz with an IF bandwidth of 1 kHz. Two additional measurements with the proprietary Asiga FusionGRAY and pre-treated FormLabs High Temperature resin have been conducted. The printed samples have a measured thickness of (0.96 ± 0.01) mm and (2.93 ± 0.01) mm, respectively.
The results for the relative complex permittivity of all three measurements are shown in figures 5(a) and 5(b), together with a literature value for PTFE [24]. The measured value $\Re\varepsilon_r$ deviates from the reference value by less than 2 %. Regarding the potential variation of material parameters due to fabrication techniques the measurement is in good agreement with the literature value. The imaginary part $\Im\varepsilon_r$ is on the same order of magnitude, but strongly varies across the frequency range. This is due to potentially systematic errors which will be discussed later.
Although $\varepsilon_r(f)$ of ASIGA FusionGRAY shows the same systematic variation it can be estimated to be $\Re\varepsilon_r = 2.68 \pm 0.03$ and $\Im\varepsilon_r = -0.07 \pm 0.03$. FormLabs High Temperature has a slightly higher real permittivity of 2.78 ± 0.01 while the imaginary part is the same within the limits of uncertainty. Compared to PTFE, both printable resins have a significantly higher real permittivity, as well as a two orders of magnitude larger absorption index k, $k_{\text{FusionGRAY}} = 0.02$ compared to $k_{\text{PTFE}} \approx 0.5 \times 10^{-3}$. Here, k is computed via $k = \sqrt{(|\varepsilon_r| - \Re\varepsilon_r)/2}$. The resins'

higher permittivity directly transfers to the refractive index, given by $n = \sqrt{(|\varepsilon_r| + \Re\varepsilon_r)/2}$, which is $n_{\mathrm{PTFE}} = 1.44$, $n_{\mathrm{FusionGRAY}} = 1.63$, and $n_{\mathrm{HighTemp}} = 1.67$.
Currently the setup only allows for characterization of isotropic, non-magnetic and low index materials. Measurements of anisotropic media are limited by the polarization-dependent coupling to the horn antennas, while magnetic samples require a different extraction method than the transmission only method in order to simultaneously determine permittivity and permeability. High index, high permittivity materials can not be tested with the current calibration technique due to the expected broad time response which cannot be properly time-gated.

5. Discussion

While first preliminary results from S-parameter measurements were found, a rigorous uncertainty analysis has to be carried out. Currently, a first estimate shows that the uncertainty in sample thickness dominates the overall uncertainty. A full Gaussian error propagation based on the error function has to be applied to achieve a better estimate in a single measurement. In addition measuring samples with different thicknesses allows for a statistical uncertainty determination.
Systematic errors have been observed in the frequency dependence. Two potential origins have been identified. First, the beam diameter incident on the sample is larger than anticipated which can lead to diffraction effects from the sample edges. A usual condition to minimize inaccuracies from diffraction is $D \geq 3w$ [13], where D is the transverse dimension of the material slab and w the beam width. In our case the slab dimension was about 1.5 times the beam size.
Second, the last far field condition is not satisfied so the sample is in the Fresnel region of the antenna, where the field pattern undergoes the transition to plane waves. This may lead to a non-planar phase front. Due to the large antenna aperture the setup has to be extended in length which in turn requires a different optical layout.
The optical system is also limited by astigmatism and aberrations. Due to the lack of radial symmetry the beam profile leaving the horn can not have a Gaussian shape. In addition the lenses' susceptibility to chromatic and spherical aberrations leads to different focal planes for the frequency points.
Another aspect to be considered is the time gating applied in the analysis of the S-parameters. Time gating requires an inverse Fourier transform, windowing in time domain and back transform to frequency domain. If the window is chosen too small the back transformed signal contains strong oscillations at the edges of the band. If the window is too large the contributions from multiple reflections in the system are not properly canceled out, and may appear as an additional periodic variation in $\varepsilon_r(f)$. Varying the span of the time gate did not reduce the periodic structure in $\varepsilon_r(f)$ presented in figs. 5(a) and 5(b). The time gate chosen here is considered to be optimal for these measurements.

The 60 GHz prismatic setup is limited by the beam size radiated from the antenna. At the exit of the prism the beam is partially clipped at large scanning angles such that the measured intensity abruptly drops during the scan, as shown in the inset of figure 2(a). The angular positioning of the scanning arm also requires a precise on-axis alignment of the prism and the rotational stage. In addition a longer scanning arm may improve the angular resolution of the intensity profile. The current scans provide broad peaks of about 20° – 30°.
The absorption measurements were not corrected for Fresnel reflections when comparing the reflected intensity of an empty line with a line including the samples. Based on the refractive indices 10 % of the incident power is reflected back to the transceiver without being attenuated in the media.
In addition the bandwidth of the emitted pulse is not specified by the manufacturer. As different

frequency components may refract under slightly different angles it is helpful for estimating the measurement uncertainty. However, the device is provided as a pulsed coherent radar for which only spatial resolution in distance measurements is specified.

In comparison, both setups result in similar values for the refractive index while the absorption is significantly different. From former studies on material dispersion in polymers [5, 11], it was not expected to observe strong changes in the refractive index between 60 GHz and 270 GHz. However, the polymers are proprietary compounds which, a priori, could be different.
Comparing the high absorption to other materials, based on the overview of dielectric properties in the millimeter range assembled by Lamb [25], the printable resins with a measured loss tangent of about $\tan\Delta\frac{\Im\epsilon_r}{\Re\epsilon_r} \approx 300 \cdot 10^{-4}$ are similar to epoxy casting resins, like Eccosorb CR 110 and Stycast 2850FT. However, epoxy resins may also show lower absorption, such as 36DA and 36DK, which indicates different chemical compositions. In comparison to other polymers such as Nylon, Polymethylmethacrylate (PMMA) or High Density Polyethylene (HDPE) [5, 25] the measured absorption is at least two orders of magnitude larger. Fedulova et al. [26] also showed that many photopolymers have a large absorption compared to non-photopolymers.
Based on the significant difference in absorption between 60 GHz and 275 GHz one may consider the approach of an absorption peak based on vibrational modes with increasing frequency. For instance, PTFE shows a significant absorption peak at 6 THz which is assigned to vibrations of CF_2 groups [27]. In case of the printable polymers studied here, the investigation of a potential peak in the absorption spectrum would require a broader spectral range.
For permittivity measurements at higher frequencies, for instance at around ~ 1 THz, THz time domain spectroscopy may be preferential due to the lack of appropriate frequency extenders for VNAs and due to the increased signal-to-noise ratio. At lower frequencies around 220 GHz this technique has a lower signal-to-noise ratio [15] which is why the VNA-based free space measurement is considered to be more suitable. It is also expected that the absorption increases towards ~ 1 THz, based on previous observations with other polymers [5, 26].
Effects of print settings on the permittivity, such as layer height, exposure time and cure time, have not yet been considered in the present work.

6. Outlook

In the near future the optical setup will be extended with two additional lenses. To minimize diffraction effects the sample will be irradiated with a smaller spot size, and the mount will be placed further away from the antennas to satisfy the far field condition. The transmission-only method will be applied to LNN calibrated measurements done in the past.
While the photopolymers studied so far are promising for transmissive devices in the V band, they are poorly applicable in the low terahertz range due to the high absorption. Further studies of a custom-made resin, which is supposed to absorb less terahertz radiation, is ongoing. Based on this new measured refractive index an axicon lens will be designed. The axicon couples the on-axis electric field in its focus region into an accelerating structure, such as a dielectric loaded waveguide or a fully dielectric photonic crystal structure.
On the long run complex geometries such as tapered waveguides [3] with an integrated coupler will be studied. Due to the unknown breakdown characteristic in the terahertz range different materials such as printable fused silica [28] may be necessary and require validation of the refractive index.

7. Conclusion

Refractive index of FormLabs Clear, FormLabs High Temperature and Asiga FusionGRAY was measured at 60 GHz as 1.609 ± 0.024, 1.648 ± 0.036 and 1.670 ± 0.015, respectively. Based on the measured dielectric permittivity, Asiga FusionGRAY shows a slightly lower refractive index

of 1.63 at frequencies around 275 GHz, while FormLabs High Temperature has a refractive index of 1.67 which is within the uncertainty of the 60 GHz result. The increase in absorption from 0.04 dB/cm at 60 GHz to about 10 dB/cm at 275 GHz for FormLabs High Temperature is significantly more than expected from the linear relation between absorption and frequency. PTFE shows a two orders of magnitude lower absorption than the cured printable resins.
Vacuum tests of pretreated prints of FormLabs High Temperature showed good results. A printed lens is in use in the ultra-high vacuum environment of SwissFEL.

Acknowledgments

The authors would like to thank M. Hünning (DESY) for fruitful discussions on free space calibration. This work has been supported in part by the Gordon and Betty Moore Foundation through the ACHIP program and by the European Research Council under the European Union's Seventh Framework Programme (FP/2007-2013)/ERC Grant Agreement n. 609920.

References

[1] Jenzer S, Auguste D, Bonis J, Delerue N, Gauthier F, Gonnin A, Trofimiuk O and Vion A 2018 *J. Phys.: Conf. Series* **1067** 082026 ISSN 1742-6588, 1742-6596
[2] Simakov E I, Andrews H L, Herman M J, Hubbard K M and Weis E 2017 Diamond field emitter array cathodes and possibilities of employing additive manufacturing for dielectric laser accelerating structures *AIP Conference Proceedings* vol 1812 (AIP Publishing) p 060010
[3] Lemery F, Floettmann K, Piot P, Kärtner F and Aßmann R 2018 *Phys. Rev. Accel. Beams* **21** 051302
[4] Mayet F 2019 *Acceleration and Phase Space Manipulation of Relativistic Electron Beams in Nano- and Micrometer-Scale Dielectric Structures* PhD Thesis University of Hamburg
[5] Busch S F, Weidenbach M, Fey M, Schäfer F, Probst T and Koch M 2014 *J Infrared Milli Terahz Waves* **35** 993–997 ISSN 18666906 iSBN: 1866-6892
[6] Weidenbach M, Jahn D, Rehn A, Busch S F, Beltrán-Mejía F, Balzer J C and Koch M 2016 *Opt. Express, OE* **24** 28968–28976 ISSN 1094-4087
[7] Hernandez-Serrano A I, Weidenbach M, Busch S F, Koch M and Castro-Camus E 2016 *J. Opt. Soc. Am. B, JOSAB* **33** 928–931 ISSN 1520-8540
[8] Busch S F, Weidenbach M, Balzer J C and Koch M 2016 *J Infrared Milli Terahz Waves* **37** 303–307 ISSN 1866-6892, 1866-6906
[9] Busch S F, Castro-Camus E, Beltran-Mejia F, Balzer J C and Koch M 2018 *J Infrared Milli Terahz Waves* **39** 553–560 ISSN 1866-6906
[10] Sathe D V 1985 *American Journal of Physics* **53** 488–490 ISSN 0002-9505, 1943-2909
[11] Elhawil A, Zhang L, Stiens J, De Tandt C, Gotzen N, Assche G and Vounckx R 2007 A quasi-optical free-space method for dielectric constant characterization of polymer materials in mm-wave band *Proceedings Symposium IEEE/LEOS Benelux Chapter* vol 66 pp 187–190
[12] Engen G F and Hoer C A 1979 *IEEE Trans. Microw. Theory Techn.* **27** 987–993
[13] Ghodgaonkar D, Varadan V and Varadan V 1989 *IEEE Trans. Instrum. Meas.* **38** 789–793 ISSN 00189456
[14] Bourreau D, Peden A and Maguer S L 2006 *IEEE Trans. Instrum. Meas.* **55** 2022–2028 ISSN 0018-9456
[15] Tosaka T, Fujii K, Fukunaga K and Kasamatsu A 2014 *IEEE Trans. THz Sci. Technol.* 1–8 ISSN 2156-342X, 2156-3446
[16] Rolfes I and Schiek B 2005 Calibration methods for microwave free space measurements *Advances in Radio Science* vol 2 (Copernicus GmbH) pp 19–25
[17] Bartley P G and Begley S B 2005 Improved Free-Space S-Parameter Calibration *2005 IEEE Instrumentationand Measurement Technology Conference Proceedings* vol 1 (Ottawa) pp 372–375
[18] Garrett D C, Bourqui J and Fear E C 2017 *Progress In Electromagnetics Research* **158** 73–87 ISSN 1559-8985
[19] Gonçalves F, Pinto A, Mesquita R, Silva E and Brancaccio A 2018 *Electronics* **7** 260 ISSN 2079-9292
[20] Dhondt G, Zutter D D and Martens L 1996 An improved free-space technique modelling for measuring dielectric properties of materials *IEEE Antennas and Propagation Society International Symposium. 1996 Digest* vol 1 (Baltimore) pp 180–183 vol.1
[21] Nicolson A M and Ross G F 1970 *IEEE Trans. Instrum. Meas.* **19** 377–382 ISSN 0018-9456
[22] Weir W B 1974 *Proc. IEEE* **62** 33–36
[23] Arslanagić S, Hansen T V, Mortensen N A, Gregersen A H, Sigmund O, Ziolkowski R W and Breinbjerg O 2013 *IEEE Antennas Propag. Mag.* **55** 91–106 ISSN 1045-9243
[24] Afsar M N 1987 *IEEE Trans. Instrum. Meas.* **IM-36** 530–536 ISSN 0018-9456, 1557-9662

[25] Lamb J W 1996 *International Journal of Infrared and Millimeter Waves* **17** 1997–2034 ISSN 0195-9271, 1572-9559
[26] Fedulova E V, Nazarov M M, Angeluts A A, Kitai M S, Sokolov V I and Shkurinov A P 2012 Studying of dielectric properties of polymers in the terahertz frequency range ed Tuchin V V, Genina E A and Meglinski I V (Saratov, Russian Federation) p 83370I
[27] Birch J R 1992 *Infrared Physics* **33** 33–38 ISSN 0020-0891
[28] Kotz F, Arnold K, Bauer W, Schild D, Keller N, Sachsenheimer K, Nargang T M, Richter C, Helmer D and Rapp B E 2017 *Nature* **544** 337–339 ISSN 0028-0836, 1476-4687